COMMUNICATIONS PHYSICS

ARTICLE

https://doi.org/10.1038/s42005-020-0348-9 OPEN

Structural trends in atomic nuclei from laser spectroscopy of tin

Deyan T. Yordanov[1,2✉], Liss V. Rodríguez[1,3], Dimiter L. Balabanski[4], Jacek Bieroń[5], Mark L. Bissell[6], Klaus Blaum[3], Bradley Cheal[7], Jörgen Ekman[8], Gediminas Gaigalas[9], Ronald F. Garcia Ruiz[2,24], Georgi Georgiev[10], Wouter Gins[11,25], Michel R. Godefroid[12], Christian Gorges[13,26], Zoltán Harman[3], Hanne Heylen[2,3], Per Jönsson[8], Anastasios Kanellakopoulos[11], Simon Kaufmann[13], Christoph H. Keitel[3], Varvara Lagaki[2,14], Simon Lechner[2,15], Bernhard Maaß[13], Stephan Malbrunot-Ettenauer[2], Witold Nazarewicz[16], Rainer Neugart[3,17], Gerda Neyens[2,11], Wilfried Nörtershäuser[13], Natalia S. Oreshkina[3], Asimina Papoulia[8,18], Pekka Pyykkö[19], Paul-Gerhard Reinhard[20], Stefan Sailer[21], Rodolfo Sánchez[22], Sacha Schiffmann[12,18], Stefan Schmidt[13], Laura Wehner[17], Calvin Wraith[7], Liang Xie[6], Zhengyu Xu[11,27] & Xiaofei Yang[11,23]

Tin is the chemical element with the largest number of stable isotopes. Its complete proton shell, comparable with the closed electron shells in the chemically inert noble gases, is not a mere precursor to extended stability; since the protons carry the nuclear charge, their spatial arrangement also drives the nuclear electromagnetism. We report high-precision measurements of the electromagnetic moments and isomeric differences in charge radii between the lowest $1/2^+$, $3/2^+$, and $11/2^-$ states in $^{117-131}$Sn, obtained by collinear laser spectroscopy. Supported by state-of-the-art atomic-structure calculations, the data accurately show a considerable attenuation of the quadrupole moments in the closed-shell tin isotopes relative to those of cadmium, with two protons less. Linear and quadratic mass-dependent trends are observed. While microscopic density functional theory explains the global behaviour of the measured quantities, interpretation of the local patterns demands higher-fidelity modelling.

[1] Institut de Physique Nucléaire, CNRS-IN2P3, Université Paris-Sud, Université Paris-Saclay, Orsay, France. [2] Experimental Physics Department, CERN, Geneva, Switzerland. [3] Max-Planck-Institut für Kernphysik, Heidelberg, Germany. [4] ELI-NP, Horia Hulubei National Institute for R&D in Physics and Nuclear Engineering, Magurele, Romania. [5] Instytut Fizyki imienia Mariana Smoluchowskiego, Uniwersytet Jagielloński, Kraków, Poland. [6] School of Physics and Astronomy, The University of Manchester, Manchester, UK. [7] Oliver Lodge Laboratory, University of Liverpool, Liverpool, UK. [8] Department of Materials Science and Applied Mathematics, Malmö University, Malmö, Sweden. [9] Institute of Theoretical Physics and Astronomy, Vilnius University, Vilnius, Lithuania. [10] CSNSM, CNRS-IN2P3, Université Paris-Sud, Université Paris-Saclay, Orsay, France. [11] Instituut voor Kern-en Stralingsfysica, KU Leuven, Leuven, Belgium. [12] Chimie Quantique et Photophysique, Université libre de Bruxelles, Brussels, Belgium. [13] Institut für Kernphysik, Technische Universität Darmstadt, Darmstadt, Germany. [14] Institut für Physik, Universität Greifswald, Greifswald, Germany. [15] Technische Universität Wien, Vienna, Austria. [16] Department of Physics and Astronomy and FRIB Laboratory, Michigan State University, East Lansing, MI, USA. [17] Institut für Kernchemie, Universität Mainz, Mainz, Germany. [18] Division of Mathematical Physics, Department of Physics, Lund University, Lund, Sweden. [19] Department of Chemistry, University of Helsinki, Helsinki, Finland. [20] Institut für Theoretische Physik II, Universität Erlangen-Nürnberg, Erlangen, Germany. [21] Technische Universität München, Munich, Germany. [22] GSI Helmholtzzentrum für Schwerionenforschung GmbH, Darmstadt, Germany. [23] School of Physics and State Key Laboratory of Nuclear Physics and Technology, Peking University, Beijing, China. [24] Present address: Massachusetts Institute of Technology, Cambridge, MA, USA. [25] Present address: Department of Physics, University of Jyväskylä, Jyväskylä, Finland. [26] Present address: Institut für Kernchemie, Universität Mainz, Mainz, Germany. [27] Present address: Department of Physics and Astronomy, University of Tennessee, Knoxville, TN, USA. ✉email: Deyan.Yordanov@cern.ch

Nuclear science greatly relies on observations, not only in naturally-occurring, but also in laboratory-synthesized nuclides, which represent the majority of approximately 3000 species discovered to date[1]. Either type can be studied by laser spectroscopy, a non-destructive experimental technique probing the hyperfine splitting of atomic energy levels induced by the nuclear electromagnetism. An electric quadrupole moment, for instance, reflects an anisotropic (deformed) charge distribution within the nucleus[2]. Appreciable nuclear deformation is primarily found in species with open shells for both protons and neutrons[3,4]. The tin isotopes, with their proton core complete (spherical), may still acquire quadrupole moments through the geometry of valence neutron orbitals. Those can be discussed in terms of schematic theoretical descriptions such as the seniority or generalized-seniority models[5,6], which explain the striking regularities previously observed, e.g., the nearly-constant energy of excited states and simple patterns exhibited by other quantities[7–9]. When looking into details, however, deviations from regular behavior are revealed as fingerprints of the underlying nucleonic shell structure and many-body correlations[10–13].

Here we study the odd-mass isotopes $^{117–131}$Sn. An $11/2^-$ state with an unpaired neutron confined by the rules of quantum mechanics to the unique-parity $h_{11/2}$ orbital is present in each case. The remaining valence orbitals in the neutron shell have the opposite parity and considerably lower angular momenta, which results in isomerism (metastability of an excited nuclear state). Quadrupole moments in the closed-shell tin isotopes are found at variance with those in the cadmium isotopes having two protons less. Differences in radii between nuclear ground and isomeric states, on the other hand, are shown to remain surprisingly similar. Calculations in the framework of nuclear density functional theory with recently optimized input describe the global behavior of the experimental observables. Interpretation of the local patterns, however, calls for a dedicated microscopic modeling.

Results and discussion

Measurements. Short-lived nuclei, naturally occurring only in astrophysical phenomena such as supernovae explosions[14], are synthesized on Earth using particle accelerators. The tin isotopes for this study were produced at the CERN-ISOLDE laboratory[15] by uranium fission using fast protons traveling with more than 90% of the speed of light. Prior conversion to neutrons increased the fission purity[16]. Tin atoms were laser ionized, accelerated to an energy of 40 or 50 keV to form a continuous beam of fast-traveling ions, and mass separated. Typically, each 100-ms segment of the beam was compressed into an ion bunch with a temporal width of less than 10 µs using a linear Paul trap[17]. Individual bunches were subsequently released, re-accelerated, and guided with a dedicated set of electrostatic optics into a volume of vaporized sodium for neutralization. Narrow-bandwidth continuous-wave laser light was introduced along the axis of ion/atom propagation. The atomic-beam energy and the associated Doppler-shifted laser frequency were defined at the sodium charge-exchange cell, whose electrostatic potential was scanned in search of resonant atomic-beam fluorescence. The latter was collected by telescopes of aspheric lenses and imaged onto the photocathodes of photomultiplier tubes for single-photon counting. The measurements were correlated with the timing structure of the atomic beam, which allowed substantial background suppression and high sensitivity. A sketch of the experimental arrangement is shown in Fig. 1a.

Laser excitation of tin atoms was performed using the two complementary transitions in Fig. 1b to resolve the nuclear properties, as described in "Methods". The laser system comprised a diode-pumped solid-state laser, a tunable laser using either dye or titanium–sapphire as the active medium, and a second-harmonic-generation cavity. Two nuclear states were detected for each odd-mass isotope in the range $^{117–131}$Sn, as shown in Fig. 2. The hyperfine structure is characterized by a sizeable quadrupole splitting in the $5p6s\,{}^1P^o_1$ state and a large magnetic splitting in the $5p6s\,{}^3P^o_1$ state. The two are correlated through the nuclear electromagnetic properties and are thus fitted simultaneously. All results are shown in Table 1. The magnetic moments therein incorporate the latest computation of the absolute shielding constant in tin[18]. The accuracy of quadrupole moments is ensured by the theoretical work outlined in the following.

Atomic structure calculations. The fully relativistic multiconfiguration Dirac–Hartree–Fock (MCDHF) method was employed to calculate the magnetic dipole hyperfine-structure constants and electric-field gradients in the $5p6s\,{}^1P^o_1$ and $5p6s\,{}^3P^o_1$ states of tin (see "Methods" for the definition of these quantities). Three independent series of large-scale calculations were performed, adopting different computational strategies and correlation models using the General Relativistic Atomic Structure Package computer codes GRASP2K[19] and GRASP2018[20], based on the same relativistic MCDHF theory and methodology[21,22]. Classes of electron excitations adopting different multireference spaces and active orbital sets were investigated in detail to clarify the role of electron correlation in the relevant matrix elements. A combined effort was put in assessing the reliability of the resulting ab initio electronic factors involved in M1 and E2 hyperfine interactions for both levels (Papoulia, A. & Schiffman, S. et al. mansuscript in preparation). The quadrupole moments from this work are obtained with the electric-field gradient 706(50) MHz/b in the singlet state, which is the mean value resulting from the aforementioned calculations. With regard to the dipole hyperfine constants in the triplet state, cross-checking calculations were performed using the configuration interaction Dirac–Fock–Sturm (CI-DFS) method[23]. The hyperfine anomaly (see "Methods") was estimated in separate multireference calculations for each isotope using a Fermi charge distribution with adopted root mean square radius and a parametrized squared harmonic-oscillator wave function of the last unpaired neutron as magnetization distribution[24]. It reaches a maximum at $^{119g}\Delta^{131m} = 0.05\%$ due to the limited overlap between the $3s$ and $1h$ nuclear wave functions and partly due to the increase in the charge radius between the two isotopes. The anomaly between positive-parity states was found to be negligible with respect to the experimental precision.

Experimental trends. The data on quadrupole moments and differences in mean square charge radii between nuclear ground and isomeric states are compared in Fig. 3 with values measured in the cadmium isotones[25–27]. A number of key observations are worth being pointed out: (i) There is a significant attenuation of the quadrupole moments of tin ($Z = 50$) with respect to cadmium ($Z = 48$). Note that the observed charge (proton) quadrupole moment originates from the nuclear response to an odd neutron in a $d_{3/2}$ or an $h_{11/2}$ single-particle state. (ii) The fitted trends in Fig. 3a, b cross each other close to zero, i.e., the $h_{11/2}$ orbital is half full[5,6] for both tin and cadmium at $N = 73$, as is $d_{3/2}$ at $N = 75$. (iii) The quadrupole moments of tin in the $11/2^-$ states are by a factor of about two larger in magnitude than those in the $3/2^+$ states. This is consistent with a stronger quadrupole polarization exerted by unique-parity $h_{11/2}$ nucleons. (iv) All trends are remarkably smooth, often near linear, at most quadratic. (v) The quadrupole moments of the $11/2^-$ states in tin exhibit a quadratic behavior with changing neutron number, strikingly different from the linear trend observed along the cadmium chain. (vi) The

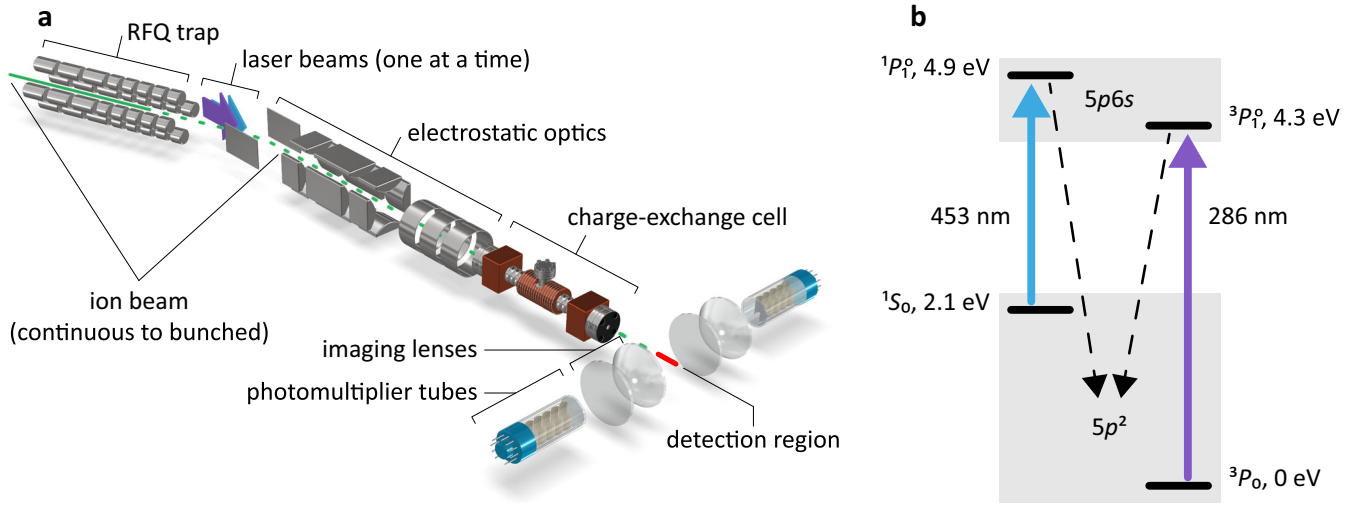

Fig. 1 Experimental arrangement and level scheme in the neutral atom of Sn. a From left to right: linear Paul trap for ion-beam bunching; continuous-wave laser beams; electrostatic elements: deflector, quadrupole triplet, cylinder lens; alkali-vapor cell; optical detection: fused-silica aspheric lenses, photomultiplier tubes. **b** Partial energy level scheme of neutral tin indicating the studied excitations and the subsequent fluorescence used for detection. The shaded areas indicate the groups of $5p^2$ and $5p6s$ levels.

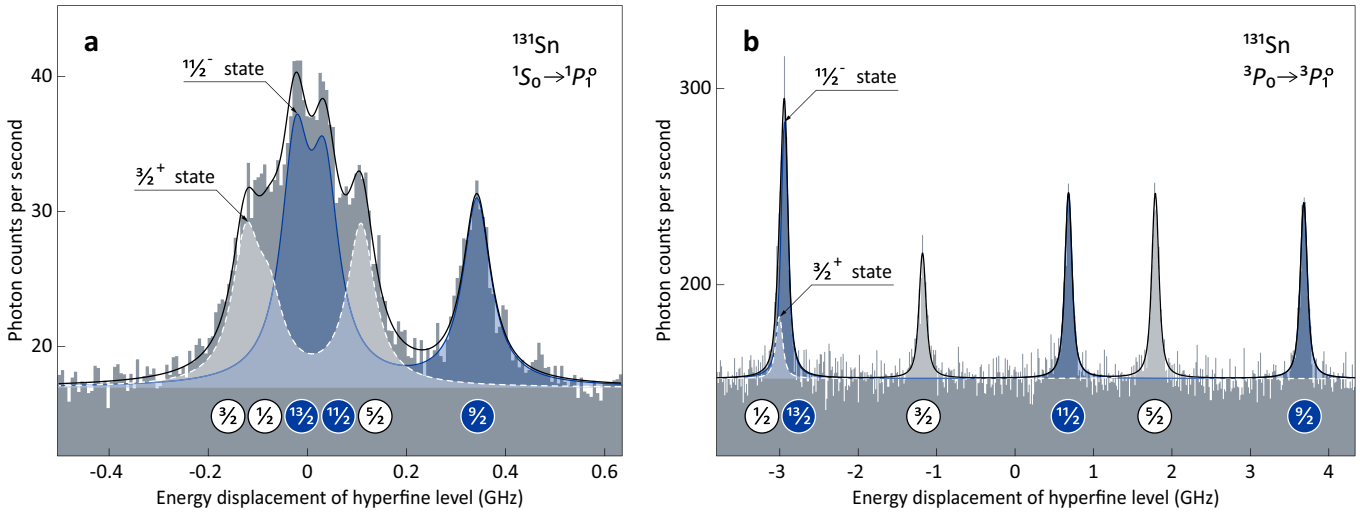

Fig. 2 Fluorescence spectra of ^{131}Sn. Hyperfine structure in the **a** $5p6s\,{}^1P_1^o$ state and **b** $5p6s\,{}^3P_1^o$ state. The fitted black curves comprise a $3/2^+$ nuclear ground state, represented by the dashed white lines, and an $11/2^-$ isomer, represented by the solid blue lines. Hyperfine levels are denoted by the individual total angular-momentum quantum number.

pattern is unexpectedly reversed for the $3/2^+$ states whose quadrupole moments change linearly for tin and quadratically for cadmium. (vii) Re-evaluated values for ^{113,115,119}Sn[28] in Fig. 3a, b are consistent with the trends defined by the heavier isotopes. These are independently calibrated to experimental γ-decay rates, thus showing consistency between nuclear data and atomic theory. (viii) The measured mean square charge-radii changes in Fig. 3c are fairly similar for tin and cadmium. All these features are discussed in the following.

Nuclear structure calculations. The theoretical analysis at the level of nuclear density functional theory[29] (DFT) employs the standard Skyrme functional SV-min[30] and the recently optimized Fayans functional Fy(Δr, HFB)[31], the latter containing gradient terms in surface and pairing energies[32,33]. Both models are optimized to the same large set of basic ground-state nuclear data[30]. In addition, Fy(Δr, HFB) accommodates the isotopic shifts of charge radii in the calcium chain, a feature which could only be achieved by invoking the Fayans gradient terms[31,34]. The calculations for the charge radius, which is an isotropic observable, were done in spherical approximation with pairing handled at Hartree–Fock–Bogoliubov (HFB) level. The odd nucleons were treated within the blocking ansatz[35]. In principle, the odd nucleon polarizes the nucleus and so perturbs the spherical shape. The impact of this polarization effect on charge radii and correlations beyond mean field are small for heavier spherical species as the tin isotopes[36,37]. To check the uncertainty from the spherical mean-field approximation, we performed more elaborate blocked HFB calculations allowing axial deformations and spin polarization for the case of the SV-min model. In this variant, each magnetic sub-state produces a slightly different radius whose average is very close to the spherical result. This supports our spherical calculations and the variance of charge radii within a *jm* shell delivers an estimate of their theoretical uncertainties.

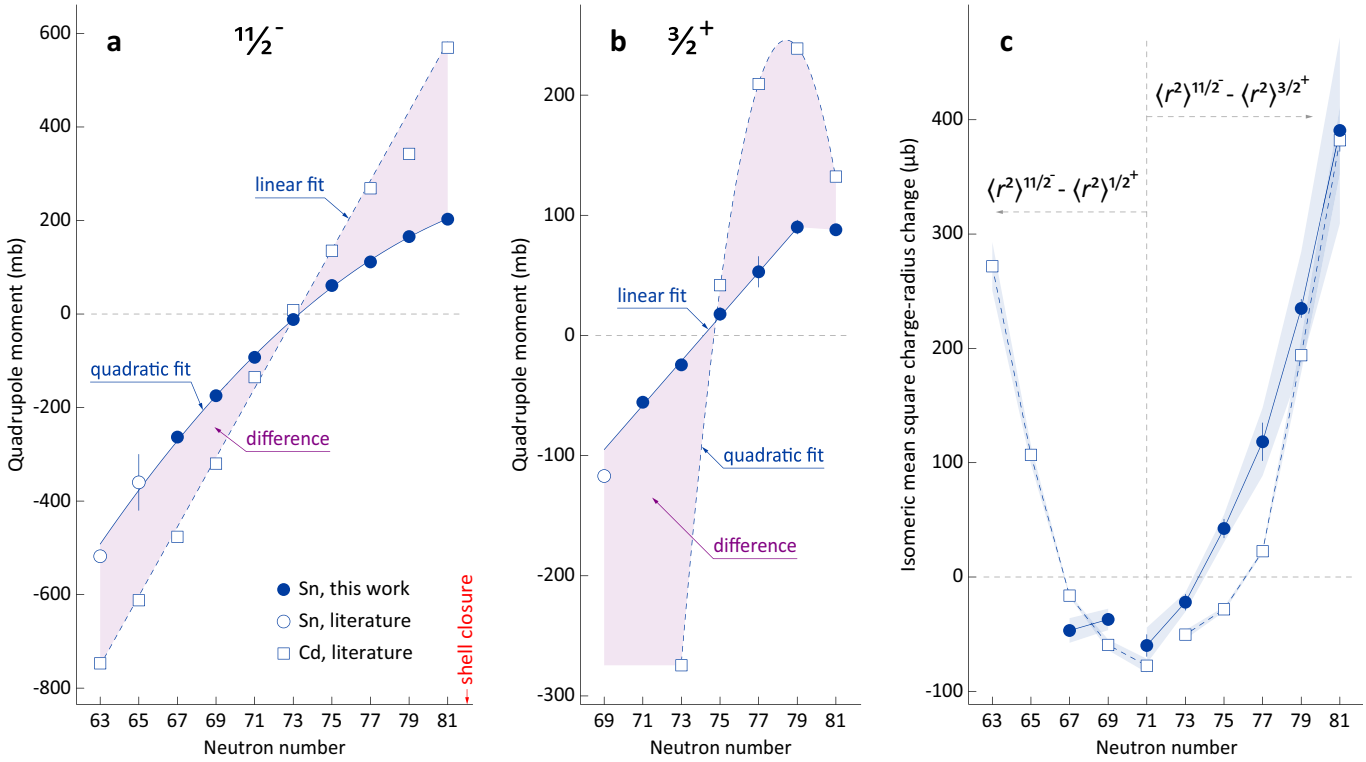

Fig. 3 Sn vs. Cd. a $11/2^-$ quadrupole moments. **b** $3/2^+$ quadrupole moments. Correlated uncertainties originating from the electric-field gradients are smaller than the dots. **c** Mean square charge-radii changes for the $11/2^-$ states relative to the $1/2^+$ ($N \leq 71$) and $3/2^+$ ($N \geq 71$) states. Shaded bands represent systematic uncertainties originating from the field-shift coefficients. The literature values are taken from refs. [25,26,28].

Figure 4a shows the quadrupole moments of $11/2^-$ states in tin and cadmium which were obtained by blocking the $m = 11/2$ magnetic substate of the $h_{11/2}$ orbital in calculations that break spherical symmetry. It is satisfactory to see that the general experimental pattern in Fig. 3a is reproduced. Namely, the quadrupole moments exhibit a smooth increase as a function of the neutron number, with the quadrupole moments of tin being reduced in magnitude relative to cadmium. The enhanced quadrupole correlations in cadmium stem from the enhanced polarizability through the two $g_{9/2}$ proton holes[38,39]. Indeed, in the nuclear shell model[40] and in nuclear DFT[41], deformation is primarily driven by the isoscalar neutron–proton (quadrupole) interaction, acting against the sphericity-favoring monopole force, which includes the isovector pairing interaction. According to the seniority coupling scheme[5–7], the spectroscopic quadrupole moment should vanish at mid-shell. In SV-min, the neutron $h_{11/2}$ shell becomes half-filled at $N = 75$, as seen in Fig. 4a. Experimentally, the zero crossover point is at $N = 73$, which suggests that the single-particle energy of the $h_{11/2}$ shell is perhaps not optimal in our model. This nicely demonstrates that the present high-precision data on quadrupole moments deliver extremely sensitive criteria for probing the shell structure of a model.

Theoretical values for the isomeric charge-radii shifts of the odd-mass tin isotopes are displayed in Fig. 4b, c. The error bars on the SV-min results indicate the estimated uncertainty of the spherical approach as compared to calculations allowing shape deformation as well as spin polarization and subsequent angular momentum projection, as explained above. We expect similar uncertainty for the Fy(Δr, HFB) model. One finds an acceptable agreement for the charge radii difference between the $11/2^-$ and the $3/2^+$ states, with a preference towards the Fy(Δr, HFB) description, especially when considering the theoretical uncertainty. This is not the case for the radii changes between the $11/2^-$ and the $1/2^+$ states, since the experimental data approach the upper end of theoretical results in Fig. 4b. A word of caution is in order here: the $1/2^+$ state is particularly prone to a dynamical coupling with low-energy quadrupole vibrations which is expected to enhance the charge radius.

The trends of quadrupole moments, linear vs. quadratic, are different for cadmium and tin owing to a significant configuration dependence. The latter does not cause a substantial deviation between the corresponding mean square charge-radii changes. The future theoretical analysis would need to address these features in greater detail together with variations of the magnetic moments shown in Fig. 5. Any connection with the quadrupole moments of the lowest 2^+ states in the even–even isotopes[42,43] should also be examined.

Perspective. Complex systems often display regular patterns. Atomic nuclei, composite structures consisting of hundreds of nucleons, are no exception; they often behave as ordered systems obeying elementary rules[5]. The reason for such simplicities is the presence of many-body symmetries resulting in a collective nucleonic motion. A challenge for the modern microscopic theory is to explain the origin of underlying symmetries.

In this work, we showed that electromagnetic properties of tin nuclei evolve from one isotope to another in a simple way: along a line or parabola. The microscopic mechanisms behind the observed behavior are rooted in many-body polarization effects. While the general trends are explained by theory, the regularities seen at high experimental resolution provide a strong motivation for further theoretical developments.

Similar effects are expected to be common for nuclei whose valence nucleons move in a unique-parity shell. Dedicated studies would be required to refine the systematics in lead and mercury

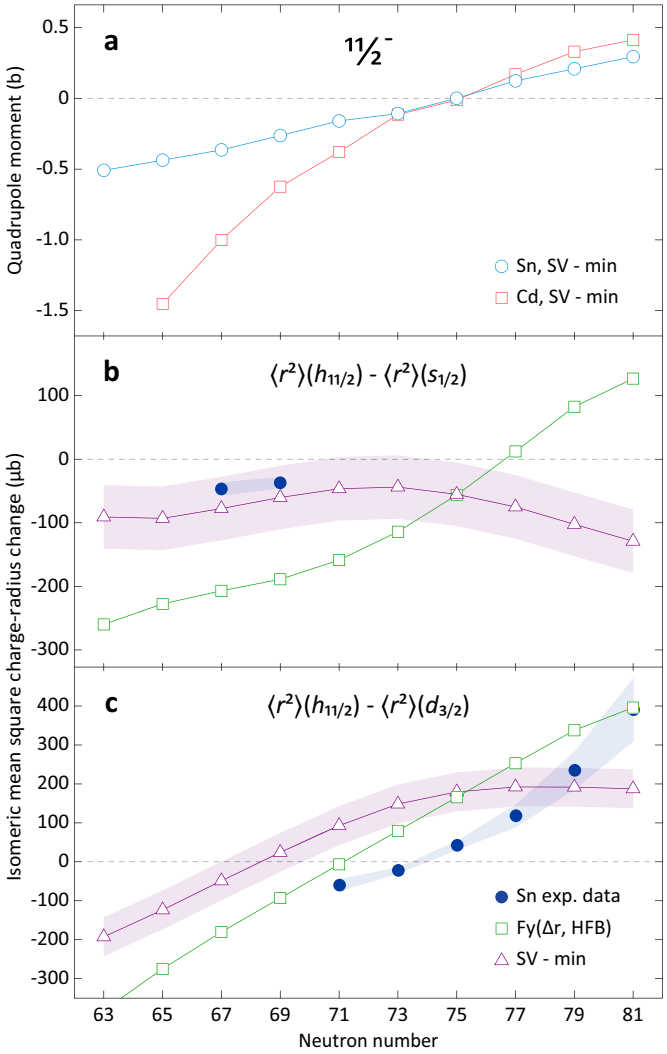

Fig. 4 Theoretical calculations. a 11/2$^-$ quadrupole moments in tin and cadmium isotopes computed with the Skyrme density functional SV-min[31]. **b**, **c** Mean square charge-radii changes for the 11/2$^-$ states relative to the 1/2$^+$ and 3/2$^+$ states in tin obtained with SV-min and the Fayans functional Fy(Δ*r*, HFB)[31].

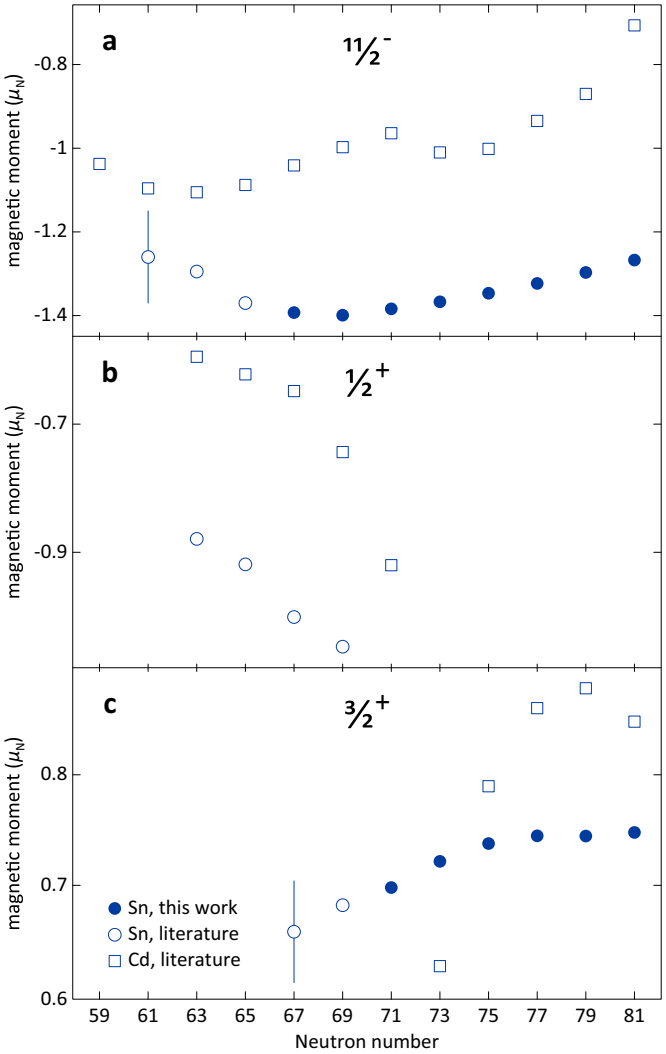

Fig. 5 Sn vs. Cd: magnetic moments. a Of the 11/2$^-$ states, **b** of the 3/2$^+$ states, and **c** of the 1/2$^+$ states. The literature values are taken from refs. [26,57]. The current high-resolution data correspond to former measurements in refs. [53,54]. The magnetic moment of the 3/2$^+$ state in ^{123}Sn is reported for the first time.

isotopes[44], which are the closest analogues of tin and cadmium in terms of nuclear structure. While initial assessments could be made by in-source measurements[45,46], the high-resolution spectroscopic techniques employed here, in combination with advanced atomic calculations, will be essential for developing further understanding of complex nuclear systems.

Methods

Hyperfine structure. The electromagnetic interaction of the nucleus with the electron environment in an atom causes splitting of the energy levels which is about a millionth of the fine-structure splitting, hence the term hyperfine structure. The energy shift of the individual hyperfine components equals

$$E_F - E_J = A\frac{k}{2} + B\frac{3k(k+1) - 4I(I+1)J(J+1)}{8I(2I-1)J(2J-1)},$$

where $A = \mu B_0/(IJ)$ is proportional to the nuclear magnetic moment μ and the average magnetic-flux density at the origin B_0, $B = eQV_{JJ}$ is proportional to the nuclear quadrupole moment Q and the average electric-field gradient at the origin V_{JJ}, $\mathbf{F} = \mathbf{I} + \mathbf{J}$ is the total angular momentum of the atom, and $k = F(F+1) - I(I+1) - J(J+1)$. The hyperfine-structure splitting is determined by the A and B parameters whose values are obtained from the experiment. The decay rate per atom, commonly referred to as Racah intensities[47], is given by

$$\frac{R}{n} = \frac{\gamma}{3\tau}\frac{(2J_1+1)(2F_1+1)(2F_2+1)}{(2I+1)(2J_2+1)}\begin{Bmatrix} J_2 & F_2 & I \\ F_1 & J_1 & 1 \end{Bmatrix}^2,$$

where τ is the lifetime of the excited atomic state and γ is the ratio between the induced and spontaneous emission coefficients, which incorporates the laser intensity and the spectral lineshape.

Hyperfine anomaly. The A hyperfine constant is influenced by the extended nuclear magnetization, known as Bohr–Weisskopf effect, and the extended nuclear charge distribution, known as Breit–Rosenthal–Crawford–Schawlow correction. Both contribute to the hyperfine anomaly:

$${}^1\Delta^2 = \frac{A_1}{A_2}\frac{I_1}{I_2}\frac{\mu_2}{\mu_1} - 1.$$

Following justification by atomic calculations, the anomaly is neglected in our analysis. However, its estimated contribution to the 11/2$^-$ magnetic moments is predicted to be on the level of the experimental precision and it is therefore incorporated into the final uncertainties quoted in Table 1, as further discussed.

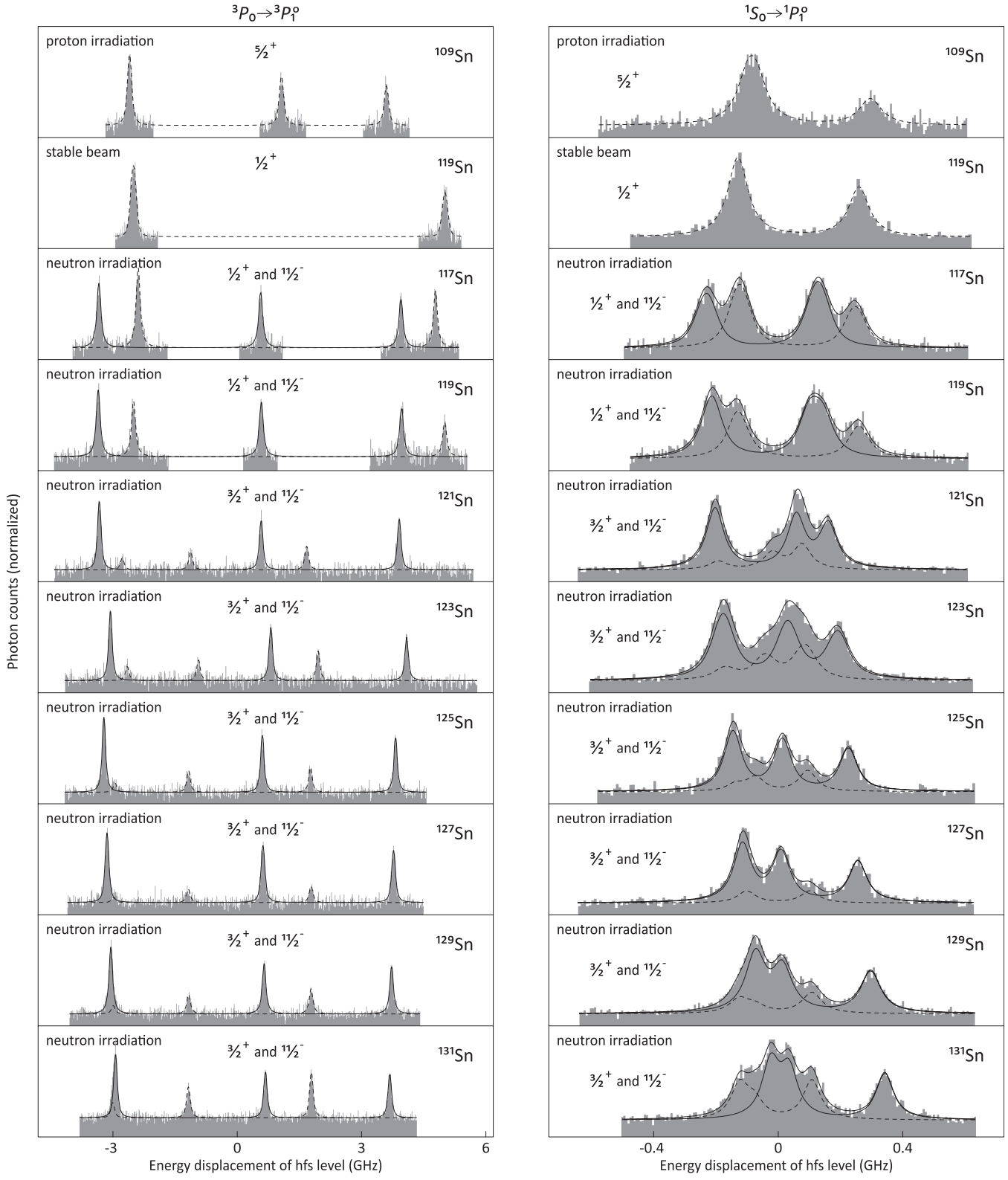

Fig. 6 Fitted fluorescence spectra of $^{109,117-131}$Sn. The common frequency scales are relative to the fine-structure splittings in the transitions $5p^2\,{}^3P_0 \rightarrow 5p6s\,{}^3P_1^o$ and $5p^2\,{}^1S_0 \rightarrow 5p6s\,{}^1P_1^o$. Positive- and negative-parity states are represented by dashed and solid lines, respectively. Solid lines in the right column also show the sum fit function. ^{119}Sn is studied from a mass marker to observe only the stable $1/2^+$ g.s., and after target irradiation to detect the radioactive $11/2^-$ state. Spectra of the stable g.s. in ^{115,117}Sn (similar to ^{119}Sn g.s.) are not shown. ^{133}Sn, used together with ^{109}Sn for calibration of the *B*-ratio, will be published elsewhere.

Table 1 Experimental results on $^{109,115-131}$Sn.

	I^π	A (MHz)	$\delta\nu^{e,o}$ (MHz)	B (MHz)	μ (μ_N)	$\delta\langle r^2\rangle^{e,o}$ (μb)	Q (mb)
^{109}Sn	$5/2^+$	−1035.8(6)		+154(5)	−1.081(1)		+218(7)(15)
^{115}Sn	$1/2^+$	−4394(2)			−0.9167(1)		
^{117}Sn	$1/2^+$	−4783(2)			−0.9983(1)		
^{117}Sn	$11/2^-$	−606.9(3)	−12(2)	−186(4)	−1.393(1)	−46(5)(11)	−263(6)(19)
^{119}Sn	$1/2^+$	−5011(3)			−1.0448(1)		
^{119}Sn	$11/2^-$	−609.6(4)	−10(2)	−123(3)	−1.399(1)	−37(5)(9)	−175(4)(12)
^{121}Sn	$3/2^+$	+1115(2)		−39(3)	+0.698(1)		−56(4)(4)
^{121}Sn	$11/2^-$	−603.0(3)	−16(3)	−65(2)	−1.384(1)	−60(10)(16)	−93(3)(7)
^{123}Sn	$3/2^+$	+1153(2)		−17(3)	+0.722(1)		−24(4)(2)
^{123}Sn	$11/2^-$	−595.7(3)	−6(2)	−8(2)	−1.367(1)	−22(7)(8)	−12(3)(1)
^{125}Sn	$3/2^+$	+1179(2)		+13(4)	+0.738(1)		+18(6)(1)
^{125}Sn	$11/2^-$	−586.8(2)	+12(2)	+43(2)	−1.347(1)	+42(8)(12)	+61(2)(4)
^{127}Sn	$3/2^+$	+1190(3)		+37(9)	+0.745(2)		+53(13)(4)
^{127}Sn	$11/2^-$	−576.6(3)	+32(5)	+79(2)	−1.323(1)	+118(17)(30)	+111(3)(8)
^{129}Sn	$3/2^+$	+1190(2)		+64(4)	+0.745(2)		+90(6)(6)
^{129}Sn	$11/2^-$	−565.1(2)	+64(2)	+117(2)	−1.297(1)	+235(8)(50)	+166(3)(12)
^{131}Sn	$3/2^+$	+1195(1)		+62(2)	+0.748(1)		+88(2)(6)
^{131}Sn	$11/2^-$	−552.2(2)	+107(1)	+143(2)	−1.267(1)	+391(4)(81)	+203(3)(14)
		$5p6s\ ^3P_1^o$	$5p^2\ ^3P_0 \rightarrow 5p6s\ ^3P_1^o$	$5p6s\ ^1P_1^o$			

$$\frac{A(^1P_1^o)}{A(^3P_1^o)} = 0.0517(2) \qquad \frac{B(^3P_1^o)}{B(^1P_1^o)} = -0.25(2) \qquad \frac{\delta\nu(^1S_0 \rightarrow {}^1P_1^o)}{\delta\nu(^3P_0 \rightarrow {}^3P_1^o)} = 0.91(2)$$

Content of each column, from left to right: isotopes; measured nuclear spins I with parity assignments π; magnetic dipole hyperfine constants A in the $5p6s\ ^3P_1^o$ state; isomer shifts relative to the unique-parity state $\delta\nu^{e,o} = \nu^{\text{odd-parity state}} - \nu^{\text{even-parity state}}$, i.e., odd "o"−even "e"; electric quadrupole hyperfine constants B in the $5p6s\ ^1P_1^o$ state; magnetic dipole moments μ in nuclear magnetons μ_N; mean square charge-radii changes relative to the unique-parity state $\delta\langle r^2\rangle^{e,o} = \delta\langle r^2\rangle^{\text{odd-parity state}} - \delta\langle r^2\rangle^{\text{even-parity state}}$; electric quadrupole moments Q with systematic uncertainties from the computed electric-field gradient and the experimental field-shift factor shown in the second sets of parentheses. In the SI system of units, 1b = 100 fm^2 = 10^{-28} m^2.

Isomer shifts. A change in the nuclear mean square charge radius between a nuclear ground state and an isomer results in a common energy displacement of all levels in a given hyperfine multiplet. The combined effect in a transition between two atomic levels is manifested in spectra from laser spectroscopy as an apparent "isomer shift". For example, in Fig. 6, this causes the pattern of peaks associated with the $11/2^-$ state in the right column to "walk" towards higher frequencies in the heavier isotopes. The isomer (frequency) shift is a product of the electronic factor, related to a change in the total electronic charge density at the site of the nucleus, and a change in the nuclear mean square charge radius:

$$\delta\nu = F_\lambda \delta\langle r^2\rangle.$$

Distinction should be made between F_λ and the total angular-momentum quantum number F introduced earlier. The effect from a change in the nuclear mass is negligible.

Fitting of multiple spectra. Routines for fitting multiple spectra were developed in the ROOT data analysis framework[48], making use of the WrappedMultiTF1 class for enveloping individual fit functions under a common χ^2. Spectra of the stable $1/2^+$ ground states in ^{115,117,119}Sn, free of quadrupole splitting, were used to determine the proportionality of A factors between the singlet and the triplet state. With this condition applied to the spectra of ^{109}Sn and ^{133}Sn, which are unperturbed by the presence of an isomer, one obtained the ratio of B factors. Individual masses were used for ground and isomeric states[49]. The isomer shifts were constrained to one another by a King plot[50] of data on the even–even isotopes. The three aforementioned ratios are presented in Table 1. Voigt line-shapes were used with a predominant Lorentzian component emerging from the fits. Resolved lines were fitted with free intensities. The heights of overlapping lines were locked to each other, or to other resolved lines when available, by using the Racah intensities. As constrained above, the fits fully determine the nuclear spins.

Nuclear properties. Using frequency ratios from the nuclear magnetic resonance of the $1/2^+$ states in ^{115,117,119}Sn[51], and the latest evaluation of the magnetic moment of ^{119}Sn[18] with an adopted uncertainty of 0.01%[52], one arrives at a high-precision magnetic moment for each of the three isotopes, as given in Table 1. These in combination with their corresponding A factors in the triplet state are used to determine the ratio $AI\mu_N/(h\mu) = 2396.6(7)$ MHz through a weighted mean, which is then used to extract magnetic moments for the rest of the isotopes. A small hyperfine-anomaly contribution of 0.05% (see the main text) is added in quadrature to the uncertainties of the $11/2^-$ magnetic moments. The quadrupole moments are determined in the singlet state with the electric-field gradient $B/(hQ) = 706(50)$ MHz/b from this work. Using the B ratio reported in Table 1, the electric-field gradient in the triplet state is found to be −173(17) MHz/b. Both are substantially stronger in comparison with semi-empirical estimates adopted in former studies[53–55]. This has had an impact on the results of a recent phenomenological analysis[56]. Mean square charge-radii changes are extracted in the triplet state with the field shift $\delta\nu/\delta\langle r^2\rangle = 0.274(57)$ MHz/μb[37].

Data availability

The authors declare that the data supporting this study are published within the paper as histograms in Fig. 6.

Received: 4 March 2020; Accepted: 2 April 2020;
Published online: 08 June 2020

References

1. Thoennessen, M. *The Discovery of Isotopes*. (Springer: Cham, Switzerland, 2016).
2. Bohr, A. & Mottelson, B. R. *Nuclear Structure*, Vol. 2 (W. A. Benjamin, Inc.: Singapore, 1975).
3. Reinhard, P.-G. & Otten, E. W. Transition to deformed shapes as a nuclear Jahn–Teller effect. *Nucl. Phys. A* **420**, 173 (1984).
4. Nazarewicz, W. Microscopic origin of nuclear deformations. *Nucl. Phys. A* **574**, 27 (1994).
5. Casten, R. F. *Nuclear Structure from a Simple Perspective*. (Oxford University Press: New York, 1990).
6. Talmi, I. *Simple Models of Complex Nuclei*. (Harwood Academic Publishers: Switzerland, 1993).
7. Talmi, I. The shell model—simplicity from complexity: some of my best nuclei are spherical. *Phys. Scr.* **92**, 083001 (2017).

8. Morales, I. O., Van Isacker, P. & Talmi, I. Generalized seniority and E2 transitions in the tin isotopes. *Phys. Lett. B* **703**, 606 (2011).
9. Stuchbery, A. E. Simple structures in complex nuclei versus complex structures in simple nuclei: a nuclear moments perspective. *J. Phys.: Conf. Ser.* **366**, 012042 (2012).
10. Morris, T. D. et al. Structure of the lightest tin isotopes. *Phys. Rev. Lett.* **120**, 152503 (2018).
11. Togashi, T., Tsunoda, Y., Otsuka, T., Shimizu, N. & Honma, M. Novel shape evolution in Sn isotopes from magic numbers 50 to 82. *Phys. Rev. Lett.* **121**, 062501 (2018).
12. Siciliano, M. et al. Pairing-quadrupole interplay in the neutron deficient tin nuclei: first lifetime measurements of low-lyingstates in ^{106,108}Sn. Preprint at https://arxiv.org/abs/1905.10313 (2019).
13. Zuker, A. P. Quadrupole dominance in light Cd and Sn isotopes. Preprint at https://arxiv.org/abs/1905.11479 (2019).
14. Burbidge, E. M., Burbidge, G. R., Fowler, W. A. & Hoyle, F. Synthesis of the elements in stars. *Rev. Mod. Phys.* **29**, 547 (1957).
15. Neugart, R. et al. Collinear laser spectroscopy at ISOLDE: new methods and highlights. *J. Phys. G* **44**, 064002 (2017).
16. Köster, U. et al. Progress in ISOL target-ion source systems. *Nucl. Instrum. Methods Phys. Res., Sect. B* **266**, 4229 (2008).
17. Mané, E. et al. An ion cooler-buncher for high-sensitivity collinear laser spectroscopy at isolde. *Eur. Phys. J. A* **42**, 503 (2009).
18. Malkin, E., Komorovsky, S., Repisky, M., Demissie, T. B. & Ruud, K. The absolute shielding constants of heavy nuclei: resolving the enigma of the ^{119}Sn absolute shielding. *J. Phys. Chem. Lett.* **4**, 459 (2013).
19. Jönsson, P., Gaigalas, G., Bieroń, J., Froese Fischer, C. & Grant, I. P. New version: Grasp2K relativistic atomic structure package. *Comput. Phys. Commun.* **184**, 2197 (2013).
20. Froese Fischer, C., Gaigalas, G., Jönsson, P. & Bieroń, J. GRASP2018—A Fortran 95 version of the general relativistic atomic structure package. *Comput. Phys. Commun.* **237**, 184 (2019).
21. Froese Fischer, C., Godefroid, M., Brage, T., Jönsson, P. & Gaigalas, G. Advanced multiconfiguration methods for complex atoms: I. Energies and wave functions. *J. Phys. B* **49**, 182004 (2016).
22. Grant, I. P. *Relativistic Quantum Theory of Atoms and Molecules. Theory and Computation*. (Springer-Verlag: NY, USA, 2007).
23. Tupitsyn, I. I. & Loginov, A. V. Use of Sturmian expansions in calculations of the hyperfine structure of atomic spectra. *Opt. Spectrosc.* **94**, 319 (2003).
24. Ekman, J., Li J., Jönsson P., Godefroid M. & Gaigalas G. Modeling hyperfine anomalies using GRASP. *Proc. EOS workshop on Electronic Atomic Factors and Hyperfine Anomalies for Nuclear Physics* (Brussels, Belgium, 2019).
25. Yordanov, D. T. et al. Spins, electromagnetic moments, and isomers of $^{107-129}$Cd. *Phys. Rev. Lett.* **110**, 192501 (2013).
26. Yordanov, D. T. et al. Simple nuclear structure in $^{111-129}$Cd from atomic isomer shifts. *Phys. Rev. Lett.* **116**, 032501 (2016).
27. Frömmgen, N. et al. Collinear laser spectroscopy of atomic cadmium. *Eur. Phys. J. D* **69**, 164 (2015).
28. Haas, H. Data re-evaluation. Private Communication (2019).
29. Bender, M., Heenen, P.-H. & Reinhard, P.-G. Self-consistent mean-field models for nuclear structure. *Rev. Mod. Phys.* **75**, 121 (2003).
30. Klüpfel, P., Reinhard, P.-G., Bürvenich, T. J. & Maruhn, J. A. Variations on a theme by Skyrme: a systematic study of adjustments of model parameters. *Phys. Rev. C* **79**, 034310 (2009).
31. Miller, A. J., Minamisono, K. & Klose, A. et al. Proton superfluidity and charge radii in proton-rich calcium isotopes. *Nat. Phys.* **15**, 432 (2019).
32. Fayans, S. A. Towards a universal nuclear density functional. *JETP Lett.* **68**, 169 (1998).
33. Fayans, S. A., Tolokonnikov, S. V., Trykov, E. L. & Zawischa, D. Nuclear isotope shifts within the local energy-density functional approach. *Nucl. Phys. A* **676**, 49 (2000).
34. Reinhard, P.-G. & Nazarewicz, W. Toward a global description of nuclear charge radii: exploring the Fayans energy density functional. *Phys. Rev. C* **95**, 064328 (2017).
35. Ring, P. & Schuck, P. *The Nuclear Many-Body Problem*. (Springer-Verlag: Berlin, 1980).
36. Hammen, M. & Nörtershäuser, W. et al. From calcium to cadmium: testing the pairing functional through chargeradii measurements of $^{100-130}$Cd. *Phys. Rev. Lett.* **121**, 102501 (2018).
37. Gorges, C. et al. Laser spectroscopy of neutron-rich tin isotopes: a discontinuity in charge radii across the $N = 82$ shell closure. *Phys. Rev. Lett.* **122**, 192502 (2019).
38. Zhao, P. W., Zhang, S. Q. & Meng, J. Explanation of the simplicity of the quadrupole moments recently observed in Cd isotopes from covariant density functional theory. *Phys. Rev. C* **89**, 011301(R) (2014).
39. Yordanov, D. T. et al. Spins and electromagnetic moments of $^{101-109}$Cd. *Phys. Rev. C* **98**, 011303(R) (2018).
40. Federman, P. & Pittel, S. Unified shell-model description of nuclear deformation. *Phys. Rev. C* **20**, 820 (1979).
41. Dobaczewski, J., Nazarewicz, W., Skalski, J. & Werner, T. Nuclear deformation: a proton–neutron effect? *Phys. Rev. Lett.* **60**, 2254 (1988).
42. Esat, M. T., Kean, D. C., Spear, R. H. & Baxter, A. M. Mass dependence of the static quadrupole moments of the first 2^+ states in the cadmium isotopes. *Nucl. Phys. A* **274**, 237 (1976).
43. Allmond, J. M. et al. Investigation into the semimagic nature of the tin isotopes through electromagnetic moments. *Phys. Rev. C* **92**, 041303(R) (2015).
44. Neyens, G. Nuclear magnetic and quadrupole moments for nuclear structure research on exotic nuclei. *Rep. Prog. Phys.* **66**, 633 (2003).
45. Ferrer, R. et al. Towards high-resolution laser ionization spectroscopy of the heaviest elements in supersonic gas jet expansion. *Nat. Commun.* **8**, 14520 (2017).
46. Sels, S. et al. Shape staggering of midshell mercury isotopes from in-source laser spectroscopy compared with density-functional-theory and Monte Carlo shell-model calculations. *Phys. Rev. C* **99**, 044306 (2019).
47. Magnante, P. C. & Stroke, H. H. Isotope shift between ^{209}Bi and 6.3-day ^{206}Bi. *J. Opt. Soc. Am.* **59**, 836 (1969).
48. Brun, R. & Rademakers, F. ROOT—an object oriented data analysis framework. *Nucl. Instrum. Methods Phys. Res., Sect. A* **389**, 81 (1997).
49. Audi, G., Kondev, F. G., Wang, M, Huang, W. J. & Naimi, S. The NUBASE2016 evaluation of nuclear properties. *Chin. Phys. C* **41**, 030001 (2017).
50. King, W. H. Comments on the article: Peculiarities of the isotope shift in the samarium spectrum. *J. Opt. Soc. Am.* **53**, 638 (1963).
51. Makulski, W. Tetramethyltin study by NMR spectroscopy in the gas and liquid phase. *J. Mol. Struct.* **1017**, 45 (2012).
52. Makulski, W., Jackowski, K., Antušek, A. & Jaszuński, M. Gas-phase NMR measurements, absolute shielding scales, and magnetic dipole moments of ^{29}Si and ^{73}Ge nuclei. *J. Phys. Chem. A* **110**, 11462 (2006).
53. Anselment, M. et al. Charge radii and moments of tin nuclei by laser spectroscopy. *Phys. Rev. C* **34**, 1052 (1986).
54. Le Blanc, F. et al. Charge-radius change and nuclear moments in the heavy tin isotopes from laser spectroscopy: charge radius of ^{132}Sn. *Phys. Rev. C* **72**, 034305 (2005).
55. Eberz, J. et al. Nuclear spins, moments and charge radii of $^{108-111}$Sn. *Z. Phys. A* **326**, 121 (1987).
56. Maheshwari, B., Abu Kassim, H., Yusof, N. & Jain, A. K. Evolution of nuclear structure in and around $Z = 50$ closed shell: generalized seniority in Cd, Sn and Te isotopes. *Nucl. Phys. A* **992**, 121619 (2019).
57. Raghavan, P. Table of nuclear moments. *At. Data Nucl. Data Tables* **42**, 189 (1989).

Acknowledgements

The authors thank the ISOLDE technical group for their professional assistance and Heinz Haas for re-evaluating the quadrupole moments of the very short-lived isomers in ^{113,115,119}Sn. This work has been supported by the Max Planck Society, the German Federal Ministry for Education and Research under Contract No. 05P15RDCIA, the Helmholtz International Center for FAIR within the LOEWE program by the State of Hesse, the Belgian IAP Project No. P7/12, the FWO-Vlaanderen, GOA 15/010 from KU Leuven, the European Union seventh framework through ENSAR under Contract No. 262010, the Science and Technology Facilities Council (ST/P004423/1 and ST/P004598/1), and by the Office of Science, U.S. Department of Energy under Grant Nos. DE-SC0013365 and DE-SC0018083 (NUCLEI SciDAC-4 Collaboration). D.L.B. acknowledges support from the EU Development Fund and Competitiveness Operational Program for the ELI-NP Project Phase II (1/07.07.2016, COP, ID1334), M.R.G. from the FWO & FNRS Excellence of Science Programme (EOS-O022818F), A.P., J.E., and P.J. from the Swedish Research Council (VR) under Contract No. 2015-04842, and P.P. from the Magnus Ehrnrooth Foundation.

Author contributions

M.L.B., R.F.G.R., C.G., H.H., S.K., V.L., S.L., S.M.-E., L.V.R., S. Sailer, L.X., X.Y., and D.T.Y. prepared the instrumentation and contributed to the on-line measurements along with D.L.B., K.B., B.C., G. Georgiev, W.G., A.K., B.M., R.N., G.N., W. Nörtershäuser, R.S., S. Schmidt, L.W., C.W., and Z.X. L.V.R. developed routines for the fitting of multiple spectra. Nuclear DFT analysis was carried out by W. Nazarewicz and P.-G.R. J.B., J.E., G. Gaigalas, M.R.G., Z.H., P.J., C.H.K., N.S.O., A.P., P.P., and S. Schiffmann contributed to the ab initio large-scale MCDHF and CI-DFS calculations of the relevant electronic parameters and to their reliability assessment. J.E. computed the hyperfine anomalies.

D.T.Y. proposed the measurements and prepared the manuscript with input from all authors. These results are part of the PhD theses of C.G. and L.V.R.

Competing interests
The authors declare no competing interests.

Additional information
Correspondence and requests for materials should be addressed to D.T.Y.

Reprints and permission information is available at http://www.nature.com/reprints

Publisher's note Springer Nature remains neutral with regard to jurisdictional claims in published maps and institutional affiliations.